Aeroelastic Simulation of HARTII Model Using Moving Overlapped Grid Approach

Shigeru Saito, Yasutada Tanabe, Choongmo Yang and Takashi Aoyama

Japan Aerospace Exploration Agency (JAXA),
7-44-1 JindaijiHigashi-machi, Chofu, Tokyo 182-8522, JAPAN
Email: ssaito@chofu.jaxa.jp
tan@chofu.jaxa.jp
yang@chofu.jaxa.jp
aoyama@chofu.jaxa.jp

Atsushi Hashimoto and Yoshiaki Nakamura

Department of Aerospace Engineering, Nagoya University,
Furo-cho, Chikusa-ku, Nagoya, Aichi 464-8603, JAPAN
Phone: +81-52-789-3394, Fax: +81-52-789-3394,
Email: hashimoto@fluid.nuae.nagoya-u.ac.jp
nakamura@nuae.nagoya-u.ac.jp

Key words : HARTII, Elasticity, CFD-CSD, Strong coupling, Moving Overlapped Grid Method

Abstract: A fluid-structure coupled simulation code has been developed to investigate aeroelastic effects of a blade on BVI noise. The flow around the blades is computed using computational fluid dynamics (CFD) with a moving overlapped grid method[1], while the blade is modeled as a beam and computed by a mode decomposition method. Mode analysis of the blade was made using Myklestad method[2][3]. Mode shapes and eigenvalues are calculated by this method and compared with HARTII data. It was shown that the frequencies of the modes agree well with the HARTII data. This method is used in the simulation using the overlapped grid as well. Strong (tight) coupling is applied for the fluid-structure coupled simulation. At the each time step, the cells are moved and deformed, according to the shape of the blade. Far-field noise is computed by an acoustic code based on Ffowcs Williams and Hawkings (FW-H) formulation[4]. The results are compared with HARTII data[5][6].

1. INTRODUCTION

Today, helicopter play a various role in the human activity, for example, life saving and disaster relief, observation around the highway and the top of volcano et al. However, as a helicopter has a chance to fly over the urban area, the noise, especially generated from main rotor in the descend flight, is extremely annoying to the neighborhood. This noise is called the ‘slap noise’ and is caused by the rotor blades striking on the tip vortices generated from the preceding blade. Such noise is referred to as Blade-Vortex Interaction (BVI) noise. The lower frequency (1-5 Blade Passage Frequency or BPF) noise was radiated by the main rotor near the plane of the rotor disk and directly ahead in the direction of vehicle translation is important for direction. Community

acceptance of rotorcraft operations is usually determined by human annoyance to the mid to high frequency (6-40 BPF) range dominated by BVI noise.

Investigation on the BVI noise has been conducted so far by so many institutes, for example NASA, ONERA, DLR, JAXA, many helicopter companies and universities et al. experimentally and CFD techniques. In 1990, the international joint cooperation within US-German and US-French MOU/MOA has been initiated. Since then, in 1994, the first wind tunnel test using German-Dutch Windtunnel (DNW) has been conducted, the main purpose was to study the effect of the Higher Harmonic pitch Control (HHC) on the BVI noise and high vibration level (called as HART project). In 2001, the second DNW test has been conducted to extend the HART data with new measurements techniques, more especially the 3-components PIV technique for wake measurements (called as HARTII project)[7]-[9]. In 2003, the HARTII data was available to the outside permitted researchers.

Concerning to CFD technique, accurate prediction of the acoustic signature associated with a main rotor system in flight is critical to civil and military applications. Because the distance of a blade relative to the vortex has a great influence on BVI noise level, correct simulation of the deformation of a blade is very important. For the accurate simulation of rotary-wing aeroelasticity, the structural analysis is combined with the CFD simulations. There are two ways to combine the fluid and structure dynamics analysis. The first method is the weak (or loose) coupling , where the fluid and structure related information is exchanged after convergence of each individual method. The second method is the so-called strong (or tight) coupling. This means that the aerodynamic loads and structural deformations are exchanged at each integral time step.

Several papers deal with the strong coupling[10][11] and weak coupling[12]-[16] have been presented so far. Altmikus et al[10] has well compared above two coupling by using the CFD code FLOWer and WAVES and comprehensive code HOST. He pointed out that the strong coupling shows almost same results with weak coupling but it takes about 2.5 times increase in cost and also it is very difficult to apply the trim calculation. Because of this inherent deficiency of the strong coupling, the loose coupling procedure is frequently used to get more accurate blade motion. The loose coupling procedure was developed by Tung, Caradonna, and Johnson using a transonic small disturbance (STD) code[17][18]. Recently the full potential methods were used later coupled. With the continual advancement of high speed computers, it becomes possible to use Euler[10][13] and Navier-Stokes[19]-[22] CFD in the coupling. Although the loose coupling strategy seems more efficient to obtain the trimmed and well converged CFD-CSD solutions, it is questionable if it can capture the strong time-dependent non-linearity such as BVI encounter or shock and stall phenomena on a blade or impulsive excitations such as quick maneuvering on small timescales.

In this paper, the strong coupling procedure is applied to investigate the effect of the blade aeroelastic behavior on the airloads of a blade. Because the BVI occurs at a very small timescale compared with one rotor rotation, it is believed that the strong coupling solution of CFD-CSD is more rigorous and promising for this problem. HARTII Model rotor was used to compare the calculated results.

2. CFD-CSD coupling Scheme

In this investigation, the CFD-CSD coupled simulation code has been developed. CFD code called the Moving Overlapped Grid Method has been used to calculate the flow around a rotor. On the other hand, structure analysis using mode decomposition method is used to calculate the blade deformation.

2.1 Numerical method

The governing equations of the aerodynamic computation are the unsteady 3-dimensional Euler equations. The inertial force terms by the rotation are included in the calculation of the blade grid[23]. Even thought it is pointed out that the strong coupling can not take account the trim calculation in the CFD procedure, the trim condition was given from other trim calculation, for example Local Momentum Theory (LMT)[24] and so on.

2.1.1 Grid system

A moving overlapped grid approach is employed to treat rotating rotor blades. The grid system for a 5-bladed configuration used in our previous study is sketched in Fig. 1. The blade grid rotates in the Cartesian background grid.

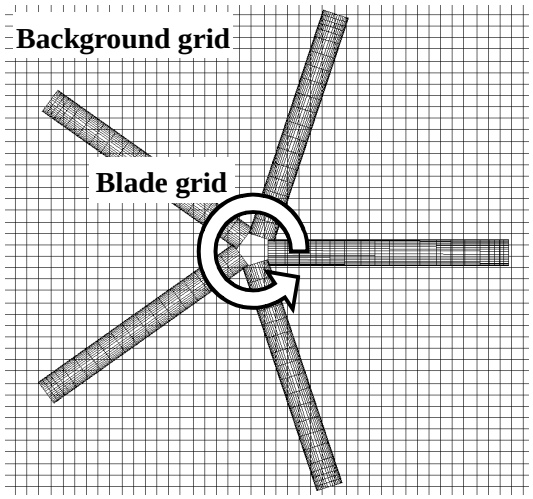

Figure 1. Blade grids and background grid for 5-bladed rotor computation.

A new grid topology is employed to concentrate grid points near the rotor disk. The Cartesian background grid is divided into the two parts as shown in Figs. 2 and 3. One is the inner background grid and the other is the outer background grid. The inner background grid is placed around the rotor disk. The outer background grid covers whole computation region and has sparse grid density. The flow data are exchanged between inner and outer background grids. The size of the two background grids for forward flight calculation is shown in Fig. 4.

Huge number of grid points is distributed to the inner background grid to achieve higher resolution, because the density of grid directly affects the strength of numerical viscosity. The blade grid wraps rotor blade using BFC and moves with the blade motions, such as rotation, flapping, feathering, and lagging. It is provided for each blade in multi-bladed computations as shown in Fig. 3. The flow data are exchanged between the blade grids and the inner background

grid at the outer boundary of the blade grids. The blade grid is generated by an algebraic formulation and has an O-H type topology. The number of grid points in span-wise direction is considerably increased to match the grid density of the blade grid with that of the inner background grid. Table 1 shows the numbers of grid points. The grid spacing of the inner background grid corresponds to 0.169c, where c is the chord length.

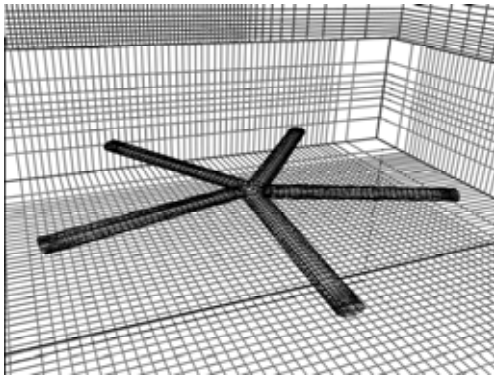

Figure 2. Blade grids, inner background grid, and outer background grid.

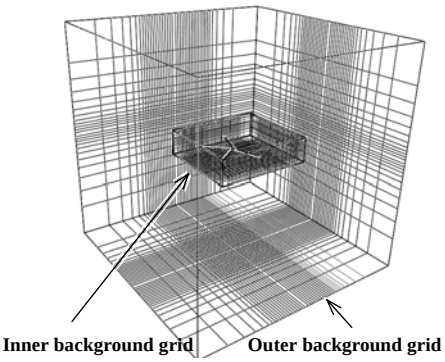

Figure 3. Blade grids and background grids.

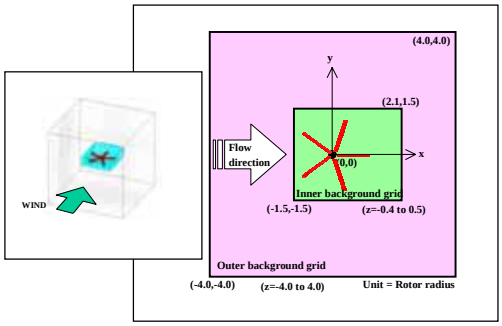

Figure 4. Size of computation regions of inner and outer background grids.

Table 1. Grid specifications.

Main Rotor	HARTII (B. L.)
Inner background grid	(x × y × z) 290 × 230 × 50 = 3,335,000
Outer background grid	(x × y × z) 83 × 79 × 49 = 321,293
Blade grid	(chord x normal x span) x blade
	(87×30×131)x4 = 1,367,640
Total	5,023,933 points
Grid spacing of Inner background grid in rotor disk	0.169c (= 0.01R)

2.1.2 Numerical method for Cartesian background grid

A high accuracy explicit scheme is utilized in the background Cartesian grid. The compact TVD scheme is employed for spatial discretization[25]. MUSCL cell interface value is modified to achieve 4th-order accuracy. Simple High-resolution Upwind Scheme (SHUS)[26] is employed to obtain numerical flux. SHUS is one of the Advection Upstream Splitting Method (AUSM) type approximate Riemann solvers and has small numerical diffusion. The time integration is carried out by an explicit method. The four stage Runge-Kutta method is used for the present calculation. The free stream condition is applied for the outer boundary of the outer background grid.

2.1.3 Numerical method for blade grid

The numerical method for the blade grid calculation is an implicit finite-difference scheme[23]. The transformed equations are written as

$$\frac{\partial \boldsymbol{Q}}{\partial \boldsymbol{t}} + \frac{\partial \boldsymbol{F_i}}{\partial \xi_{\boldsymbol{i}}} + \boldsymbol{H} = 0 \tag{1}$$

$$\boldsymbol{Q} = \boldsymbol{J}^{-1}\begin{pmatrix} \rho \\ \rho \boldsymbol{u}_1 \\ \rho \boldsymbol{u}_2 \\ \rho \boldsymbol{u}_3 \\ \boldsymbol{e} \end{pmatrix},\ \boldsymbol{F_i} = \boldsymbol{J}^{-1}\begin{pmatrix} \rho \boldsymbol{U_i} \\ \rho \boldsymbol{u}_1 \boldsymbol{U_i} + \xi_{\boldsymbol{i},1\boldsymbol{p}} \\ \rho \boldsymbol{u}_2 \boldsymbol{U_i} + \xi_{\boldsymbol{i},2\boldsymbol{p}} \\ \rho \boldsymbol{u}_3 \boldsymbol{U_i} + \xi_{\boldsymbol{i},3\boldsymbol{p}} \\ (\boldsymbol{e}+\boldsymbol{p})\boldsymbol{U_i} + \xi_{\boldsymbol{i},t\boldsymbol{p}} \end{pmatrix},\ \boldsymbol{H} = \boldsymbol{J}^{-1}\begin{pmatrix} 0 \\ -\rho\Omega \boldsymbol{u}_2 \\ \rho\Omega \boldsymbol{u}_1 \\ 0 \\ 0 \end{pmatrix}. \tag{2}$$

In these equations,

$$(\ )_{,t} = \frac{\partial}{\partial \boldsymbol{t}},\quad (\ )_{,j} = \frac{\partial}{\partial \boldsymbol{x}_j},\quad (\boldsymbol{x}_1, \boldsymbol{x}_2, \boldsymbol{x}_3) = (\boldsymbol{x}, \boldsymbol{y}, \boldsymbol{z}),\quad (\xi_1, \xi_2, \xi_3) = (\xi, \eta, \zeta),$$
$$(\boldsymbol{u}_1, \boldsymbol{u}_2, \boldsymbol{u}_3) = (\boldsymbol{u}, \boldsymbol{v}, \boldsymbol{w}),\quad (\boldsymbol{U}_1, \boldsymbol{U}_2, \boldsymbol{U}_3) = (\boldsymbol{U}, \boldsymbol{V}, \boldsymbol{W}). \tag{3}$$

The quantity ρ is the density, $\boldsymbol{u}, \boldsymbol{v}$ and $\boldsymbol{w}$ are the velocity components in the Cartesian coordinate system, and $\boldsymbol{U}, \boldsymbol{V}, \boldsymbol{W}$ are the contravariant components of the velocity. The quantity Ω is the angular velocity of the blade rotation, and $\boldsymbol{p}$ is the pressure which is represented as

$$\boldsymbol{p} = (\gamma - 1)\left(\boldsymbol{e} - \frac{1}{2}\rho \boldsymbol{u}_i^2\right) \tag{4}$$

Where γ is the ratio of specific heat and $\boldsymbol{e}$ is the total energy per unit volume. The quantity $\boldsymbol{J}$ is the Jacobian of the transformation between Cartesian and computational coordinate.

The numerical method to solve the governing equations is an implicit finite-different scheme. The Euler equations are discretized in the conventional delta form using the Euler backward time differencing. A diagonalized ADI method based on an upwind flux-split technique is used for the implicit left-hand-side regarding the spatial differencing. In addition, a higher-order upwind

scheme based on TVD is applied for the inviscid terms of the explicit right-hand-side. Each ADI operator is decomposed into the product of lower and upper bidiagonal matrices by using diagonally dominant factorization. In addition, an upwind scheme based on TVD by Chakravarthy and Osher is applied for the inviscid terms of the explicit right-hand-side. Each operator is decomposed into the product of lower and upper bi-diagonal matrices by using diagonally dominant factorization. The accuracy of this solver in space and in time is 2nd-order and 1st-order, respectively. In order to obtain the unsteady solution in forward flight conditions, the Newton iterative method is also used. In order to reduce the residual at each time-step, six iterations are used.

The typical dividing number along the azimuthal direction is about 5,000 per revolution for the HARTII blades. It corresponds to azimuth angle about 0.072°. The unsteady calculation is impulsively started from the azimuth angle of 0°.

2.1.4 Interpolation of flow data

The search and interpolation to exchange flow data, $\boldsymbol{Q} = (\rho, \rho u, \rho v, \rho w, e)^t$, between the grids are executed in each time step because the blade grid rotates with the rotor blade in the background grids. The computation time spent for search and interpolation is one of the disadvantages of the moving overlapped grid approach. In our computation, this problem is severe because a vector and parallel computer is used. Therefore, a new algorithm using tri-liner interpolation is developed and it is vectorized and paralellized[31]. The typical calculation time for the interpolation is about 20% of all calculation time in the parallel computation of 5-bladed rotor case.

2.1.5 Noise analysis

The prediction method of the far field acoustic pressure is based on the combination of CFD technique with an acoustic equation solver. Although direct computation can be used to get the noise solution directly from the flow calculation with CFD based methods, this is available only in the near field in spite of huge computing cost. At present, the best way is the coupling with the integral method for far-field prediction. Acoustic analogy[27], which is re-arranged into the Ffowcs Williams-Hawkings equation, is widely used and still under construction for better applications. Retarded time solution to this equation, neglecting quadruple noise, can be written in the form of Formulation1 by Farassat[28][29].

The prediction of rotor noise is conducted in the following procedures: 1) calculation of sound pressure of the noise source, 2) acoustic prediction computation at the observer position, and 3) post-processing of the noise data in the way of sound level using visualization or audible converting.

Hypothesis of the Ffowcs-Williams and Hawkings equation[2] to be satisfied are known that the noise source must lay in low speed flow, and the observer should be located outside of the source region (i.e. outside of the boundary layer, separation flow or wake) in order to avoid the nonlinear effect. In most calculations to compare the results with wind tunnel experiment, the observer moves in the same direction and at the same speed as the noise source. The pressure distribution on the blade surface calculated by the CFD code is stored every 0.5 degrees in azimuth-wise

direction as the input data in noise calculation.

The acoustic pressure p, which is the function of an observer position x and an observer time t, satisfies the wave equation as follows:

$$\left(\frac{1}{c^2}\frac{\bar{\partial}^2 p}{\partial t^2}-\bar{\nabla}^2 p\right)\cdot H(f)=-\left(\hat{p}_n+\frac{1}{c}M_n\hat{p}_t\right)\delta(f)-\frac{1}{c}\frac{\bar{\partial}}{\partial t}\{M_n\hat{p}\delta(f)\}-\bar{\nabla}\cdot\{\hat{p}n\delta(f)\} \tag{5}$$

where $H(f)$ is the Heaviside function and $\delta(f)$ is the Dirac delta function. The quantity c is the speed of sound. The bar over the operator symbol denotes operators involving generalized derivatives[29]. The vector n and $M_n, \hat{p}, \hat{p}_n,$ and $\hat{p}_t$ in equation (5) are described as follows:

$$n=\nabla f,\ M_n=\frac{1}{c}\frac{\partial f}{\partial t},\ \hat{p}=\lim_{f\to+0}p(x,t),\ \hat{p}_n=\nabla\hat{p}\cdot\nabla f,\ \hat{p}_t=\frac{\partial\hat{p}}{\partial t}. \tag{6}$$

By using the Green function in unbounded space, equation (5) gives

$$p(x,t)\cdot H(f)=\int_{-\infty}^{t}d\tau\int G^0\left\{-\left(\hat{p}_n+\frac{1}{c}M_n\hat{p}_t\right)\delta(f)-\frac{1}{c}\frac{\partial}{\partial t}[M_n\hat{p}\delta(f)]-\nabla\cdot[\hat{p}n\delta(f)]\right\}dy \tag{7}$$

where

$$G^0(y,\tau\,|\,x,t)=\frac{1}{4\pi r}\delta(g), \tag{8}$$

and

$$g=\tau-t+\frac{r}{c}. \tag{9}$$

In equation (7), the vector y is a source position, τ is a source time. In equation (9), r is the distance between a source and an observer position. By performing the integration on the influential surface in equation (7), the following equation is obtained.

$$4\pi p(x,t)\cdot H(f)=-\int\frac{\hat{p}_n+M_n\hat{p}_t/c}{r\Lambda}d\Sigma+\int\frac{\hat{p}\cos\theta}{r^2\Lambda}d\Sigma+\frac{1}{c}\frac{\partial}{\partial t}\int\frac{(\cos\theta-M_n)\hat{p}}{r\Lambda}d\Sigma \tag{10}$$

where

$$\Lambda=\sqrt{1+M_n-2M_n\cos\theta} \tag{11}$$

In equation (10), Σ is the influential surface generated by all Γ-curves as the source time τ varies $-\infty$ to t for the fixed observer position x and time t, where the Γ-curve is the intersection of body and sphere $g=0$. The function g is defined by equation (9) and $g=0$ shows the sphere on which the acoustic pressure transmits in the space. The quantity θ is the angle between n and r [30]. Figure 6 shows the schematic view of the influential surface. In the figure 7, the chart of the acoustic analysis used in this investigation is shown.

2.1.6 Treatment of blade motion

The aerodynamic blade deformations such as flapping, torsion, and lead-lag deformations are

calculated at each time step in CFD calculation. These deformations are calculated by using mode decomposition method. Mode calculation was performed by using the Myklestad method. In this method, a blade is composed of several discrete masses and bays. Each bay has structural properties such as flapping bending stiffness, EI_y and the chordwise bending stiffness, EI_z and torsional stiffness, GJ. The blade torsional, flap bending, and chordwise bending equations of equilibrium can be derived respectively as follows:

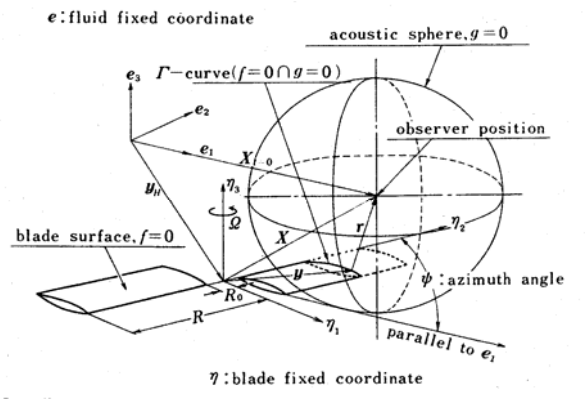

Figure 6. Schematic view of the influential surface.

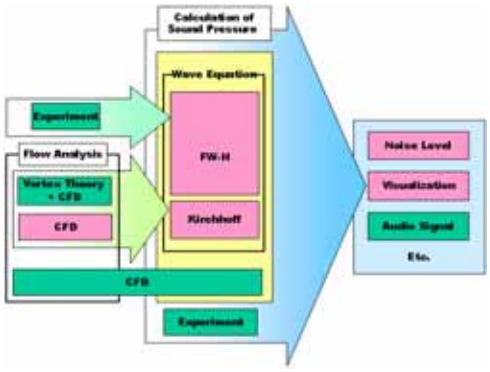

Figure 7. The chart of acoustic analysis.

$$
\begin{aligned}
&-[(GJ + Tk_A^2)\phi']' + (EI_z - EI_y)\left[(w''^2 - v''^2)\frac{\sin 2\theta}{2} + v''w''\cos 2\theta\right] \\
&+ mk^2(\ddot{\phi} + \Omega^2\phi) + me[\ddot{w} - \theta\ddot{v} + \theta\Omega^2 v + e\Omega^2\phi + r\Omega^2(w' - \theta v')] \\
&= M_{ax} - m[eg + k^2(\ddot{\theta} + \Omega^2\theta + 2\Omega\theta\dot{v}')] + e\theta(e_0\Omega^2 - 2\Omega\dot{u})]
\end{aligned}
\tag{12}
$$

$$
\begin{aligned}
&\left[\{EI_y + (EI_z - EI_y)\sin^2\theta\}w'' + (EI_z - EI_y)\left(\frac{v''\sin 2\theta}{2} + \phi v''\cos 2\theta + \phi w''\sin 2\theta\right)\right]'' \\
&-(Tw')' + m(\ddot{w} + e\ddot{\phi}) \\
&= F_{az} - m(g + e\ddot{\theta} - e\Omega^2\theta)
\end{aligned}
\tag{13}
$$

$$
\begin{aligned}
&\left[\{EI_z + (EI_z - EI_y)\sin^2\theta\}v'' + (EI_z - EI_y)\left(\frac{w''\sin 2\theta}{2} - \phi v''\sin 2\theta + \phi w''\cos 2\theta\right)\right]'' \\
&-(Tv')' + m[\ddot{v} - e\theta\ddot{\phi} - \Omega^2(v - e\theta\phi)] \\
&= F_{ay} + m[-2\Omega\dot{u} + 2e\Omega(\dot{v}' + \theta\dot{w}') + e\theta\ddot{\theta} + \Omega^2(e_0 + 2e)]
\end{aligned}
\tag{14}
$$

When the coupled mode shapes and the associated frequencies are denoted by $\bar{w}, \bar{v}, \bar{\phi}$ and ω_j, respectively, blade deformations can be expressed as

$$
w = \sum_{j=1}^{\infty}\bar{w}_j \cdot q_j, \quad v = \sum_{j=1}^{\infty}\bar{v}_j \cdot q_j, \quad \phi = \sum_{j=1}^{\infty}\bar{\phi}_j \cdot q_j \tag{15}
$$

Where q_j is the generalize coordinate of the j^{th} coupled mode. According to the Rayleigh-Ritz approach[31], equations (12)-(14) result in the following form where the orthogonality condition of the natural modes was used in the derivation.

$$M_j\left\{\frac{d^2q_j}{dt^2}+\omega_j^2\cdot q_j\right\}=Q_j \quad (j=1,2,3\cdots) \tag{16}$$

Where M_j and Q_j are a generalized mass and generalized force respectively shows as follows:

$$M_j=\int_0^R[(k^2\bar{\phi}_j+e\bar{w}_j-e\theta\bar{v}_j)\bar{\phi}_j+(\bar{w}_j+e\bar{\phi}_j)\bar{w}_j+(\bar{v}_j-e\theta\bar{\phi}_j)\bar{v}_j]mdr \tag{17}$$

$$\begin{aligned}Q_j=&\int_0^R[\{M_{ax}-m[eg+k^2(\ddot{\theta}+\Omega^2\theta+2\Omega\theta\dot{v}')+e\theta(e_0\Omega^2-2\Omega\dot{u})]\}\bar{\phi}_j\\&+\{F_{az}-m(g+e\ddot{\theta}-e\Omega^2\theta)\}\bar{w}_j+\{F_{ay}+m[-2\Omega\dot{u}+2e\Omega(\dot{v}'+\theta\dot{w}')\\&+e\theta\ddot{\theta}+\Omega^2(e_0+2e)]\}\times\bar{v}_j]dr\end{aligned} \tag{18}$$

The radial extension of the blade u is approximated as

$$\begin{aligned}u&=r-\int_0^r[1+v'^2+w'^2]^{\frac{1}{2}}dr\\&\cong-\frac{1}{2}\int_0^r[v'^2+w'^2]dr\\&=\sum_{j=1}^{\infty}\bar{u}_j\cdot q_j\end{aligned} \tag{19}$$

where

$$\begin{aligned}u&=-\int_0^r w_0'\bar{w}_j'dr\\w_0&=\text{trim value of } w\end{aligned} \tag{20}$$

In order to take into the account of preconing angle β_0 of a blade, the aerodynamic forces and moments are change as follows:

For the flapwise correction: $F_{a,z} \Rightarrow F_{a,z}-\bar{m}_j r_j\Omega^2\cos(\beta_0)\sin(\beta_0)$

For the torsional correction: $M_{a,x}\Rightarrow M_{a,x}-F_{a,z}e_{EA}-e_{CG}\bar{m}_j r_j\Omega^2\cos(\beta_0)\sin(\beta_0)$

Where $F_{a,z}, M_{a,x}$ are the normal aerodynamics force and pitching moment respectively. Also e_{EA}, e_{CG} are the distance between elastic axis and aerodynamics center (quarter chord) (Positive toward leading edge) and between elastic axis and center of gravity (positive toward leading edge). The inertial forces by these dynamic motions have not considered yet in the present flow solver.

2.9 Calculation conditions

HARTII blade is selected in this calculation. The HARTII model rotor was positioned on the lateral center of the DNW test section, and 915 mm up from the longitudinal centerline (Fig. 8). The dimensions of the calculated rotor and the operating conditions are summarized in Tables 2 and 3. In this investigation, only Baseline case of the HARTII data was used because the main purpose of this investigation was developing the CFD-CSD code by using the Moving Overlapped Grid Method with the mode decomposition method.

Figure 8. HARTII hingeless rotor model in DNW Wind tunnel

Table 2: Dimensions of blades

Main Rotor	HARTII (B.L.)
Number of blades, b	4
Rotor Radius, R (m)	2.0
Chord Length, c (m)	0.121
Blade Twist, θ_t (deg/R)	-8.0
Aspect Ratio, AR	16.5
Airfoil	NACA23012mod

For the Mode analysis, The Holtzer Myklestad method was used to calculate the eigenvalues and eigenvectors. The blade structural property of the HARTII model were used.

Table 3: Operating conditions

Main Rotor	HARTII (B.L.)
Tip Mach Number, M_{Tip}	0.6387
Advance ratio, μ	0.15
Shaft tilt angle, $\imath_s$	5.3 deg.(aft)
Preconing angle, β_0	2.5 deg.
Collective pitch angle, θ_0	3.20 deg
Lateral Cyclic pitch angle, θ_{1c}	-2.0 deg
LongitudinalCyclic pitch angle, θ_{1s}	1.1 deg

3. Results and Discussions

Mode analysis was executed by the Myklestad method. Calculated results are shown in Table 4. Results are compared with those by other papers. In this figure, 1st and 2nd natural frequencies are well coincident with those of HARTII blade and other papers. However for above 3rd mode, present calculation results shows different tendency compared with other results. In the case of 3rd mode, present results show the torsion mode, however HARII data shows the flap mode and Umac or Boyd data show the flap/torsion mode. The present results also shows the strong coupling with the flap mode, therefore it may be called as flap/torsion mode in this case. In the case of 5th mode, present result and the results by other papers shows the torsion 3rd mode, however HARTII data shows the 3rd lead-lag mode. After more precise investigation, this 3rd torsion mode is strongly coupled with lead-lag motion. With the precise comparison, the present calculation results show the almost same blade property that is expressed by the other means.

Table 4. Natural Frequencies of HARTII blade.

	Natural Mode Frequency (/rev)			
Mode Number	Umarc	Boyd et al	HARTII	Present Method
1(Lead-Lag)	0.787	0.786	0.782	0.754
2(Flap)	1.11	1.111	1.125	1.138
3(Torsion)				2.66
3(Flap)			2.835	
3(Flap/Torsion)	2.8	2.8		
4(Torsion)	4.06	4.43	3.845	3.82
5(Torsion)	4.607	4.604		4.366
5(Lead-lag)			4.592	
6(Lead-lag)				4.697
6(Flap)	5.058	5.03	5.168	
7(Flap)	7.794	7.806		6.665
8(Flap)	11.171	11.199		9.237
9(Lead-lag)				11.056
10(Torsion)				11.603

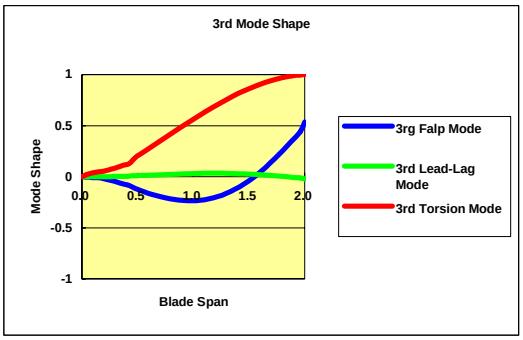

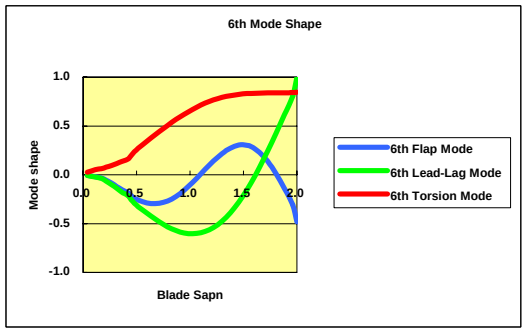

(a) 3rd mode shape **(b) 6th mode shape**

Figure 9. Comparison of 3rd and 6th mode shape

First of all, these natural frequencies and natural vectors are applied to the LMT. This theory calculates the instantaneous momentum balance between momentum lift and blade element lift and finally derives the local lift on a blade. These aerodynamic forces and moments are combined with the structural calculation. The LMT was calculated at each 10 degrees time step and at the

same time the structural calculation was executed by using the aerodynamic forces in the generalized forces.

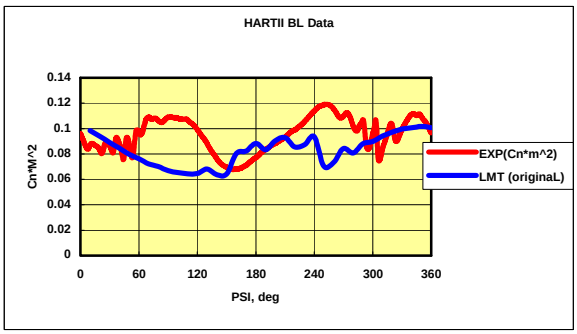

Figure 10. Comparison of the Blade pressure fluctuation.

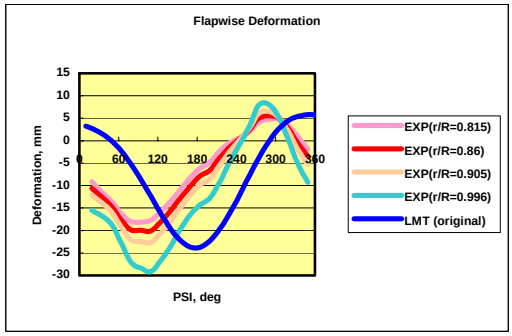

Figure 11. Comparison of the flap deformation of the HARTII data with LMT results.

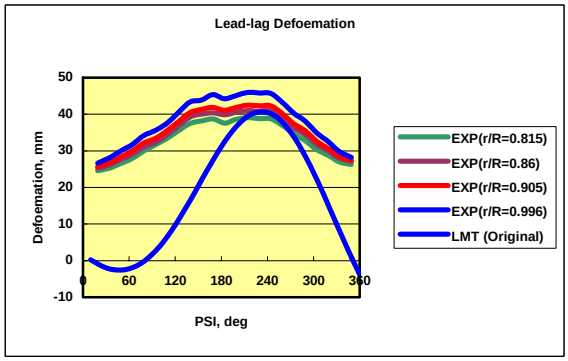

Figure 12. Comparison of the lead-lag deformation of the HARTII blade with LMT results

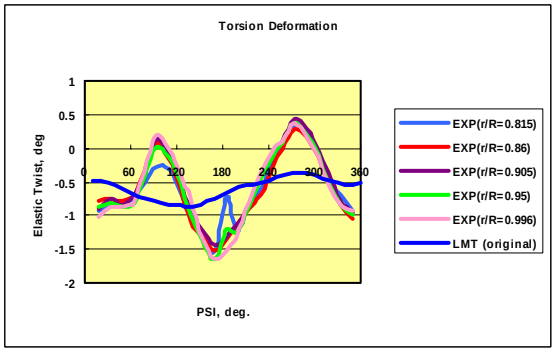

Figure 13. Comparison of the torsion deformation of HARTII blade with LMT results

Figure 10 and figure 13 show the comparison of the HARTII data with LMT results. Concerned with the lift fluctuation at the spanwise position of r/R=0.87, LMT results shows that general tendency is coincident with the HARTII data, however the BVI events can not be captured. On the other hand, blade aeroelastic deformations shows good agreement with HARTII data in magnitude and phase. However in the case of the torsional deformation. LMT result cannot show the 2or 3p vibratory property.

In the case of CFD-CSD analysis, above blade property (eigenvalues and eigenvectors) are used to solve the blade aeroelastic deformation. The calculation of the aeroelastic deformation is performed at each time step in CFD, namely about 5,000 steps per one revolution in shown figure 17. This CFD-CSD combined calculation was started after rotor without blade deformations would reach the convergent stage, almost 5 revolutions, then the CSD code was combined with the CFD code.

Figure 15(a) shows the iso-vorticity contour around a rigid-blade rotor. Also figure 15(b) shows the comparison of lift fluctuation of HARTII data with CFD result. About the Iso-vorticity, tip vortices disappear around azimuthal angle 70 to 80 degrees in the advancing side and also 270 to 300 , where the BVI events have well happened (see figure 15(b).) The reason of this discrepancy

is not clear at this present time.

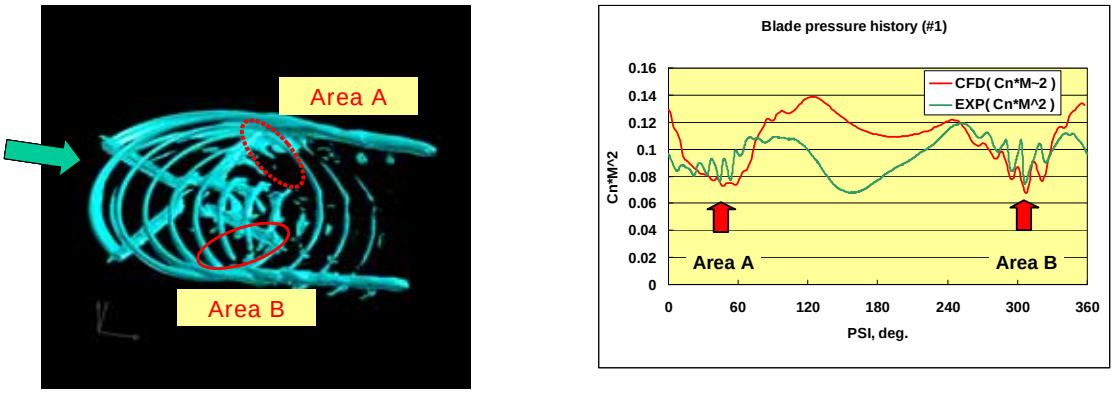

(a) Iso-vorticity contour around a rotor **(b) Comparison of Lift fluctuation of a blade**

Figure 15. Iso-vorticity contour and comparison of Lift fluctuation by CFD .

Figure 16(a) and (b) show the noise carpet contour below the rotor of HARTII data and CFD calculation respectively. Even though the CFD calculation does not include an effect of the blade deformation, a noise carpet property shows well coincidence with the HARTII data. As shown in this figure, BVI events are mainly occurred in 1st quadrant and 4th quadrant. CFD calculation shows well coincidence with the HARTII data.

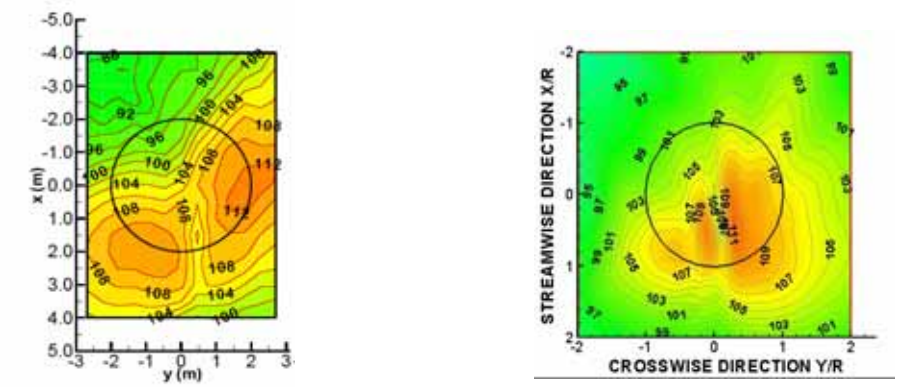

(a) Carpet noise contour below a rotor **(b) Carpet noise contour by CFD**

Figure 16. Comparison of the carpet noise contour of HARTII below a rotor data and CFD.

Figure 17 shows the flow chart of present CFD-CSD coupling analysis. In this calculation, the structure analysis is executed at the each time step in CFD calculation. The calculation was started after the 6 revolutions in which a blade was supposed to be a rigid blade. Even though time interval was so small in CFD, a blade have sudden deformation. As a result, a fairly large deformation in flap and torsion direction can be seen and each blade has different response at the beginning. It is necessary to get the same response for each blade. At the present time, it takes long time to get such convergence status in this strong coupling system. From the investigation using the strong coupling procedure, several important issues to be improved, such as viscous effect, trim calculation, inertial terms due to blade deformation have been clear. Concerning to the trim calculation, it should be investigate the weak (or loose) coupling.

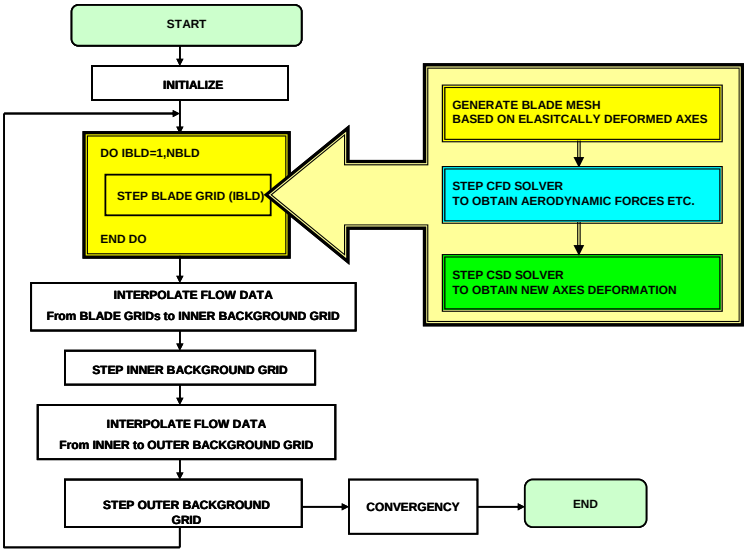

Figure 17. Flow chart of the CFD-CSD coupling.

4. Conclusions

The CFD-CSD coupling code has been developed by combination with the Moving Overlapped Grid Method (CFD part) and the mode decomposition method (CSD part). This code has been executed by using the HARTII data. Through this investigation, the following conclusions have been derived.

(1) CSD analysis is combined with CFD code, the Moving Overlapped Grid Method to investigate the aeroelastic effect on the blade airloading and acoustic property.
(2) Mode analysis was made by the Myklestad method.
(3) Results of the eigenvalues are well coincident with HARTII data and other analysis.
(4) CFD code shows the accurate airloadings on a blade.
(5) Numerical calculations shows the great sensitivity with CSD coupling.

5. Future Works

In this CFD-CSD coupling study to get accurate airloadings of a blade, several important assumption, such as no viscosity and so on, have imposed in these calculations. Therefore the following items have to be considered.

(1) Inertial effects by blade deformation should be included.
(2) Viscous effect should be included. (Navier Stokes Equations will be used.)
(3) Weak coupling should be considered from the trim calculation point of view.
(4) The prescribed blade deformations should be included to enhance the time efficient calculation.

6. Acknowledgement

The authors wish to thank the HARTII team for their help and for the data and valuable insights. Authors would like to thank Dr.-Ing., M.S. Berend G. van der Wall for his kind support of HARTII data, and Dr. Casey Burly and Dr. Chee Tung for their suggestion to participate in the HARTII workshop and valuable discussion about the HARTII data.

7. References

[1] Ochi, A., et al: Parallel Numerical computation of Helicopter Rotor by Moving Overlapped Grid Method, AHS International Meeting on Advanced Technology and Disaster Relief, 1998.

[2] Myklestad, N.O., Fundamentals of Vibration Analysis, McGraw-Hill Book Company inc., New York, 1944.

[3] Myklestad, N.O., A New Method of Calculation Natural Modes of Uncoupled Bending Vibration of Airplane Wings and Other types of Beams, J. of Aeronautical Sciences, April, 1944.

[4] Ffowcs Williams, J.E. et al, Sound Generation by Turbulence and Surface in Arbitrary Motion, Philosophical Trans. of the Royal Society of London, Series A, Vol.264, 1969, pp.21-342.

[5] van der Wall, B., 2nd HHC Aeroacoustic Rotor Test (HART II), - Part I: Test Documentation -, Braunschweig, 2003.

[6] van der Wall, B., 2nd HHC Aeroacoustic Rotor Test (HART II), - Part II: Representative Results -, Braunschweig, 2003.

[7] Yung, H.Y., Tung, C., van der Wall, B., Pausder, H.-J., Burley, C., Brooks, T., Beaumier, P., Delrieux, Y., Merker, E. and Pengel, K., The HART-II Test: Rotor Wakes and Aeroacoustics with Higher-Harmonic Pitch Control (HHC) Inputs – The Joint German/French/Dutch US Projects -, 58th American Helicopter Society Annual Forum, Montreal, Canada, June 11-13, 2002.

[8] Lim, J.W., Tung, C., Yung, H. Yu, Burely, C., Brooks, T., Boyed, D., Bernard van der Wall, Schneide, O., Richard, H., Raffel, M., Beaumier, P., Bailly, J., Delrieux, Y., Pengel, K. and Merker, E., HART-II: Prediction of Blade-Vortex Interaction Loading, 29th European Rotorcraft Forum, Friedrichharfen, Germany, 16-18 September, 2003.

[9] Baill, J., Delrieux, y. Beaumier, P., HARTII : Experimental Analysis and Validation of ONERA Methodology for the Prediction of Blade-Vortex Interaction, 30th European Rotorcraft Forum, Marseilles, France, September, 2004.

[10] Altmikus, A.R.M., Wagner, S., Beaumier, P., and Servera, G., A comparison: Weak versus Strong Modular Coupling for Trimmed Aeroelastic Rotor simulations, American Helicopter Society 58thAnnual Forum, Montreal, Quebec, June,2002.

[11] Poinot, M., Costes, M., and Cantaloube, B., Application of CGNS software components for Helicopter blade Fluid-Structure Strong Coupling, 31st European Rotorcraft Forum, Florence, Italy September, 2005.

[12] Beaumier, P., A Coupling procedure Between a Rotor Dynamics Code and a 3D Unsteady Full potential Code, American Helicopter Society 3rd Decennial Specialists' Conference on Aeromechanics, San Francisco, CA, January 1994.

[13] Servera, G., Beaumier, P., and Cosres, M., A Weak Coupling Method between the Dynamics Code HOST and the 3DUnsteady Euler code WAVES, 26th European Rotorcraft Forum, The Hague, Netherlands, September 2000.

[14] Sitaraman, J., Coupled CFD/CSD prediction of Rotor Aerodynamic and Structural Dynamic Loads for Three Critical Flight condition, 31st European Rotorcraft Forum, Florence, Italy, September 13-15, 2005.

[15] Sim, W.W. and Lim, J.W., Blade-Vortex Interaction (BVI) Noise & Airload prediction using Loose Aerodynamic/Structural coupling, 62nd American Helicopter Society annual Forum, Phoenix, Arizona, 2006.
[16] Gopalan, G., Sitaraman, J., Baeder, J.D. and Schmitz, F.H., Aerodynamic and Aeroacoustic Prediction Methodologies with Application to the HARTII Model rotor, 62nd American Helicopter Society annual Forum, Phoenix, Arizona, 2006.
[17] Strawn, R.C., Desopper, F.X. and Miller, M. and Jones, A., Correlation of PUMA Airloads, Paper No. 14, 15th European Rotorcraft Forum, Amsterdam, Netherlands, September 1989.
[18] Strawn, R.C. and Bridgeman, J.O., An Improved Three-Dimensional Aerodynamics Model for Helicopter Airloads Prediction, AIAA Paper 91-0767, AIAA 29th Aerospace Sciences Meeting and Exhibit, Reno, NV, January, 1991.
[19] Sitraman, J., Beader, J., and Chopra, I., Validation of UH-60A Rotor Blade Aerodynamic Characteristics Using CFD, American Helicopter Society 59th Annual Forum, Phoenix, AZ, May, 2003.
[20] Sitraman, J., Datta, A., Beader, J.D., and Chopra, I., Fundamental Understanding and Predictuion of Rotor Vibratory loads in High-Speed Forward Flight, 29th European Rotorcraft Forum, Friedrichhafen, Germany, September, 2003.
[21] Pahlke, K. and van der Wall, B., Calculation of Multibladed Rotors in High-Speed Forward Flight with weak Fluid-Structure-Coupling, 27thEuropean Rotorcraft Forum, Moscow, Russia, September 2001.
[22] Datta, A., Sitraman, J., Chopra, I., and Beader, J., Improved comprehensive analysis for Prediction of Rotor Vibratory Loads in High-Speed Forward Flight, American Helicopter Society 60th Annual Forum, Baltimore, MD, June 2004.
[23] Kondo, N., Ochi, A., Nakamura, H., Aoyama, T., Saito, S. and Yamakawa, E., Validation of Rotor Aerodynamic and Acoustic Prediction Methods using ATIC 2nd Model Rotor, 26th European Rotorcraft Forum, The Hague, Netherlands, 2000.
[24] Azuma, A. and K. Kawachi, K., Local Momentum Theory and Its Application to a Rotary Wing, AIAA 75-865, 1975.
[25] Yamamoto, S., et al: Journal of Computers & Fluids, Vol.22, pp.259-270, 1993.
[26] Shima, E., et al: Role of CFD in Aeronautical Engineering (No.14) – AUSM type Upwind Scheme -, NAL SP-34, 1996.
[27] Lighthill, M.J., On sound Generated Aerodynamically: I. General Theory, Proceedings of the Royal Society of London, Series A: Mathematical and Physical Sciences, Vol.211, No.1107, 1952, pp.564-587.
[28] Farassat, F., Theory of Noise Generation from Moving Bodies with an Application to Helicopter Rotors, NASA TR R-451, 1975.
[29] Farassat, F.,: Discontinuities in Aerodynamics and aeroacoustics: The concept and Applications of Generalized Derivatives, Journal of Sound and Vibrations, Vol.55, No.2, 1977.
[30] Nakamura, Y., et al, Rotational Noise of Helicopter Rotors, Vertica, Vol.3, No.3/4, 1979, pp.293-316.
[31] Kanichiro Kato and Takashi Yamane, A Calculation of Rotor Impedance for Hovering Articulated-Rotor Helicopters, Vol. 16, No. 1, January 1979, pp.15-22.